Forest SAR Tomography

Principles and applications

HOSSEIN AGHABABAEI, GIAMPAOLO FERRAIOLI, LAURENT FERRO-FAMIL, YUE HUANG, MAURO MARIOTTI D'ALESSANDRO, VITO PASCAZIO, GILDA SCHIRINZI, AND STEFANO TEBALDINI

Synthetic-aperture radar (SAR) systems are widely used for monitoring vegetation and forested environments. Those that offer large-scale coverage, short revisiting times, and an under-foliage wave-penetration capability have been broadly employed to extract information about the forest structure. Similarly, 3D forest structures that serve as important indicators of productivity and biomass levels can be efficiently estimated using the SAR tomography (TomoSAR) processing technique through multibaseline (MB) image acquisition. This article provides an overview of the main developments in forest TomoSAR during the past two decades.

MONITORING FORESTED AREAS

Characterizing and monitoring forested areas are highly important activities for tracking climate change and quantifying the global carbon cycle in the form of aboveground-biomass (AGB) mapping. Forest environments play profound roles in resource utilization, ecology, and biodiversity applications [1], a fact that highlights the significance of monitoring them. Forest characterization is mainly associated with the identification of its vertical structure, which typically represents the arrangement of the trees, trunks, and crown. The forest structure constitutes a significant indicator of productivity and biomass level and thus is recognized by the scientific community as a major element in forest monitoring [2]–[4]. Structure variation can reveal the dynamics of the forest, and the temporal evolution of the AGB distribution can be inferred from monitoring the forest structure at a global scale [5].

In situ forest monitoring provides the most accurate data parameters but involves expensive and time-consuming field work. Remote sensing techniques have the advantage of consistent, large-scale coverage and short revisiting times that can ease the difficulties that are encountered with traditional approaches. Remote sensing techniques that guarantee under-foliage penetration capabilities and enable 3D measurements (not only the horizontal variability but the vertical parameter) are best suited to forest monitoring.

High-resolution waveform lidar and TomoSAR [6] are the two most popular approaches to 3D forest monitoring, and their different sensing technologies result in advantages and drawbacks for each. Among them, the remarkable advantages of SAR, which is almost independent of weather conditions due to the ability of microwaves to penetrate semitransparent media and cover a larger study area, have

Digital Object Identifier 10.1109/MGRS.2019.2963093
Date of current version: 12 February 2020

drawn the attention of the scientific community. However, in SAR images, the 3D-sensed information is projected into a so-called azimuth-range 2D domain. TomoSAR overcomes this issue by exploiting several images to reconstruct the radar reflectivity's 3D distribution. The key aspect of this advanced technique involves synthesizing an array along the vertical direction to measure the backscattering characteristics of the scene along the elevation direction and, hence, generate a full 3D image. Thanks to a great deal of research, TomoSAR is now an operational tool, and the link between the reconstructed 3D radar reflectivity and the physical forest structure is well established and understood [7]–[9]. In particular, this technique offers a unique geo-biosphere tool to carry out accurate 3D reconstruction and provide reliable biophysical information for forested areas, including vertical structure and biomass. It is comparable to conventional tools, such as the terrestrial and lidar approaches, for forest monitoring.

©ISTOCKPHOTO.COM/ONFOKUS

This article provides a concise overview of TomoSAR with a particular reference to forest applications. It covers the evolution of tomographic processing techniques with single and multiple polarimetric data sets. We begin with insight into the core of TomoSAR and the major estimation and reconstruction methods that have emerged during the past two decades. For each case, experimental results from real data are provided to give readers application scenarios for the techniques and an overview of TomoSAR processing's potential and limits. Table 1 outlines the article's structure. In it, the important references to different topics are presented.

INSIGHT INTO TOMOSAR

SAR is a well-established tool for the generation of high-resolution, day-and-night, 2D images, independent of weather conditions. The contribution of each target in the image can be represented by two coordinates: the azimuth and slant range (x, r). The azimuth refers to the platform track direction, while the slant range may be thought of as the line-of-sight (LOS) direction and denotes the distance between the platform and target. Generally, due either to the side-looking nature of SAR systems or the penetration of the microwave signal into semitransparent media, the 3D world is projected into the 2D azimuth-range image. With reference to forest environments, where the ground and upper layer of the backscattering are coherently superimposed into a resolution cell, monitoring the vertical structure may not be feasible with 2D imaging.

TomoSAR, with its vertical-resolution capability, is an MB processing approach that has overcome the limitation

of 2D imaging. The TomoSAR principle returns to the basic concept of MB interferometry, where the acquisition space is enhanced by different trajectories to form a synthetic aperture along the third dimension (see Figure 1).

TABLE 1. THE FOREST TOMOSAR FRAMEWORK.

TOMOSAR SIGNAL MODEL AND RECONSTRUCTION	
TomoSAR overview and focusing approaches ("Insight Into TomoSAR" section)	• Physical view and the concept [6], [10] • Signal model [10], [11] • TomoSAR processing and reconstruction approaches [10]–[13]
PolTomoSAR ("Pol TomoSAR" section)	• Polarimetric signal model [9], [11], [14] • Reconstruction framework [14]–[16] • MB polarimetric target scattering decomposition [17]–[20]
INHERENT PROBLEMS	
The main difficulties of TomoSAR processing ("Inherent Difficulties of TomoSAR" section)	• Nonoptimal MB SAR sensor configurations [6], [10], [21] • Phase-error issues and calibration methods [22]–[25] • Temporal decorrelation and possible remedies [26]–[28]
APPLICATIONS	
Applications of TomoSAR across forest environment ("Application Examples" section)	• Biomass mapping [29]–[31] • Under-foliage parameter extractions and ground/digital terrain model generation [31], [32]
FUTURE TRENDS	
Overview of the advances and looking into the future ("Conclusions" section)	

This direction, referred to as the *cross range* (ζ), is shown in Figure 1; it is orthogonal to the LOS and sensor trajectory. From the given geometry in Figure 1, ζ may be straightforwardly connected to the vertical direction through $z = \zeta \sin(\theta)$. For an SAR system to be sensitive to elevation (through ζ), two or more images of the same area must be acquired and jointly processed. Hence, the synthesis of the array along the cross-range direction enables the estimation of the 3D backscattering map in the (x, r, ζ) reference system. This map can be translated to the standard coordinate system of the azimuth, ground range, and elevation through a simple rotation.

The MB system's ability to locate targets in 3D space mainly depends on the number of acquisitions and the baseline distribution. Its effectiveness for resolving targets in the elevation dimension is directly connected to the synthetic antenna in the same direction, which constitutes all the available sensors. The interferometric phase difference between the master and slave images is determined only by the geometry of the acquisition as $\Delta\phi = k_z \times z$, where z is the elevation of the point-like scattering target and k_z is called the *vertical wavenumber* or *phase-to-height conversion factor*, which is defined in (3) later in the article. The sensitivity of the interferometric phase to the vertical direction is ruled by k_z, which, in turn, increases with the distance between sensors. Large k_z magnitudes provide a high sensitivity to the vertical direction but reduce the unambiguous range of the elevations that can be recovered. Any phase measurement lies in the $(-\pi, \pi)$ interval spanning a height range that is expressed by $Ha = 2\pi/k_z$ and referred to as the *height of ambiguity*.

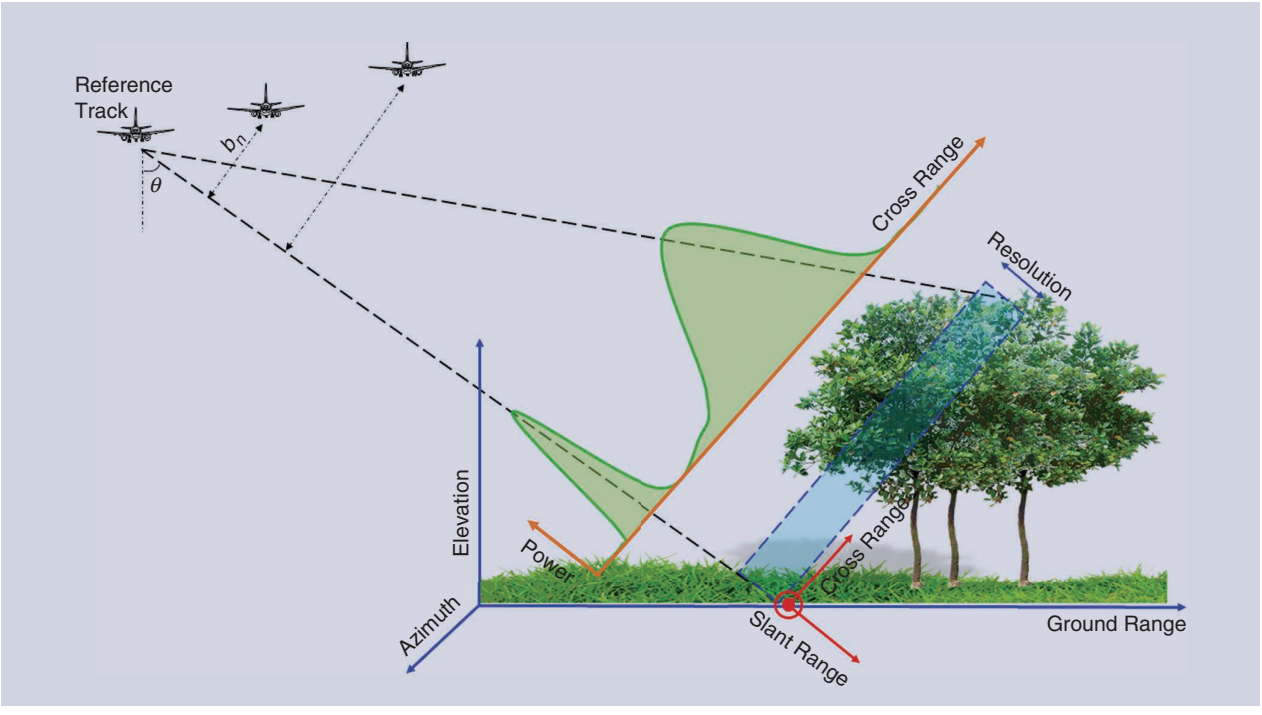

FIGURE 1. The MB TomoSAR geometry and 3D voxel-resolution cell (x, r, ζ).

TOMOSAR SIGNAL MODEL

Let us refer to the geometry of the MB SAR imaging system, where N SAR images along different orbits, not necessarily coplanar and uniformly spaced, are acquired across the same target area. The classical focusing algorithm is applied to obtain 2D, full-resolution, single-look complex (SLC) SAR images from raw data in each track. Let's assume that the SLC images are co-registered with subpixel accuracy to the reference master image. After the co-registration step, the information associated to a single target appears in the same pixel in all of the images. The co-registration step usually follows the selection of an image (the master) of the stack to set the reference geometry. Hence, for a fixed pixel (with x and r coordinates), the generic model of the *nth* element in the data-stack vector, $\mathbf{y} \in \mathbb{C}^{N\times 1}$, is given by [6], [10]

$$y_n(x,r) = \int_{-\Delta\zeta}^{\Delta\zeta} \gamma(x,r,\zeta) e^{-i\frac{4\pi}{\lambda}[\rho_n(x,r,\zeta)-\rho_n(x,r,0)]} d\zeta + w_n, \quad (1)$$

where $\rho_n(x,r,\zeta)$ represents the distance between the scatterer located at position (x,r,ζ) and the *nth* sensor. The exponential factor highlights the so-called de-ramping compensation, $2\Delta\zeta$ expresses the extension of the cross range in the imaged scene, γ represents the scene's scattering properties, and w_n represents the complex additive noise.

After expanding the difference $\rho_k(\zeta) - \rho_k(0)$, associating the ζ-dependent term in γ, and moving from the cross range to the elevation in accordance with $z = \zeta \sin(\theta)$, the discretized version of the TomoSAR equation in correspondence to any (x, r, z) coordinate can be derived by sampling in L steps as

$$\mathbf{y} = \sum_{l=1}^{L} \gamma(z_l)\mathbf{a}(z_l) + \mathbf{w}, \quad (2)$$

where the dependence of the data-stack vector $\mathbf{y}$ on (x,r) has been neglected for the sake of notation simplicity. The steering vector $\mathbf{a}(z_l) = [e^{ik_{z1}(z_l)}\, e^{ik_{z2}(z_l)} \ldots e^{ik_{zN}(z_l)}]^T$, with T as transpose operator, is constructed by the two-way vertical wavenumber (k_{zn}) between the master and *nth* acquisition tracks, defined as

$$k_{zn} = \frac{4\pi}{\lambda}\frac{b_n}{r\sin(\theta)}, \quad (3)$$

where γ and b_n denote the system wavelength and perpendicular baseline of the *nth* image with respect to the master. Let $\boldsymbol{\gamma} = [\gamma(z_1)\gamma(z_2)\ldots\gamma(z_L)]^T \in \mathbb{C}^{L\times 1}$ be the unknown discrete function that contains L uniformly spaced, unknown samples; (2) can be written in the linear form as

$$\mathbf{y} = \mathbf{A}(\mathbf{z})\boldsymbol{\gamma} + \mathbf{w}, \quad (4)$$

where $\mathbf{A} \in \mathbb{C}^{N\times L}$ is a steering matrix that contains L steering vectors. Several inversion techniques exist to retrieve the unknown reflectivity function $\boldsymbol{\gamma}$ in (4); a detailed overview of these approaches is presented in the next section. We note that the complex additive-noise vector $\mathbf{w}$ in (4) follows a Gaussian distribution with zero mean and a standard deviation of σ_w.

Some remarks are now in order. The factor $2\Delta\zeta$ in (1) and consequently in (4) plays a key role in the inversion process. To identify the reconstructed signal, the solution space should be restricted to the range of the height of ambiguity given by the Nyquist interval, that is, $2\Delta\zeta = \lambda r/2\bar{b}_n$, where $\bar{b}_n$ is the mean baseline separation between the acquisitions. It is worth highlighting that the ideal discrete version of (1) is obtained by uniformly sampling ζ through the illuminated scene's cross-range extension, with the sampling step being lower than the Nyquist-resolution value. In particular, the cross-range Nyquist resolution $\delta\zeta$ can be derived based on the overall length of the orthogonal baseline (B_n), given by

$$\delta\zeta = \frac{\lambda r}{2B_n}. \quad (5)$$

RECONSTRUCTION APPROACHES

The purpose of the tomographic-reconstruction techniques presented in this section is to estimate γ from the measurements $\mathbf{y}$ or, rather, the vertical backscatter intensity $|\gamma|^2$. Under the hypothesis of uncorrelation along z of the vertical-reflectivity profile (that is, $E\{\gamma(z)\gamma(s)^\dagger\} = \delta(z-s)|\gamma(z)|^2$), the second-order statistics of the MB measurements $\mathbf{y}$ can be expressed as

$$\mathbf{R} = E\{\mathbf{y}\mathbf{y}^\dagger\} = \mathbf{A}(\mathbf{z})\mathbf{R}_\gamma\mathbf{A}(\mathbf{z})^\dagger + \sigma_w^2\mathbf{I} \in \mathbb{C}^{N\times N}, \quad (6)$$

where $\mathbf{R}$ and $\mathbf{R}_\gamma = \text{diag}\{|\boldsymbol{\gamma}|^2\}$ represent the covariance matrices of $\mathbf{y}$ and $\boldsymbol{\gamma}$, respectively, and $\mathbf{I}$ is the identity matrix. In the equations presented so far, $E, \delta, \dagger$, and $\text{diag}\{.\}$ denote the expectation, delta function, Hermitian operators, and diagonal operators, respectively.

Equation (6) states that each element of the covariance matrix of the random vector $\mathbf{y}$ represents an estimation of the Fourier transform of the vertical reflectivity profile $|\boldsymbol{\gamma}|^2$. This feature implies that the problem of estimating the scene's 3D structure amounts to a spectral-estimation problem. During the past decades, many algorithms have been developed for estimating the spectrum of a signal; some of them are described in this section, with considerations of the physical assumptions they rely on.

Spectral-estimation algorithms can be divided into two main groups: model-free (nonparametric) and model-based (parametric). Model-based algorithms have significant features that can describe the forest layer. Conversely, model-free approaches do not rely on any a priori knowledge of the vegetation layer and can result in a more flexible reconstruction. The vertical structure of a vegetation layer is often described in terms of the vertical distribution of the ensembles' backscattering, which can be classified based on their polarimetric signature. Most models include a mixture of contributions from the ground and canopy [33]. Generally speaking, the former is highly concentrated along the vertical direction (a Dirac delta, in the limit case

of infinite bandwidth), whereas the latter spreads throughout a larger range of elevations with more polarimetric randomness. However, the exact features of each scattering mechanism and their relative weights depend on many factors, including the tree species, moisture, and wavelength. Hence, to capture the physical phenomenon, a large set of parameters is needed, which makes the model difficult to invert. Because of these issues, model-free approaches are usually preferred when dealing with forests; two widely used algorithms are detailed throughout the remainder of this section: the beamforming algorithm and the Capon spectral estimator [12].

The beamforming and the Capon methods aim to find a filter vector $\mathbf{h}$ to project the MB data $\mathbf{y}$ such that the reflectivity from a specific scatterer situated at elevation z_l is recovered, while the echoes of the scatterers placed at different elevations are rejected. The beamforming algorithm achieves this goal by constraining the minimum norm of $\mathbf{h}$ mathematically

$$\mathbf{h}_{\mathrm{BF}} = \min_{\mathbf{h}} \mathbf{h}^{\dagger}\mathbf{h} \quad \text{s.t.} \quad \mathbf{h}^{\dagger}\mathbf{a}(z_l) = 1. \tag{7}$$

The solution to this problem is given by $\mathbf{h}_{\mathrm{BF}} = \mathbf{a}(z_l)/N$, where the filtered signal's retrieved power is given by

$$\mathbf{P}_{\mathrm{BF}}(z_l) = \frac{\mathbf{a}^{\dagger}(z_l)\mathbf{R}\mathbf{a}(z_l)}{N^2}. \tag{8}$$

The resolution along the elevation of the beamforming algorithm is limited and connected to the baseline distribution; also, sidelobes in the vertical impulse-response function (IRF) inject backscattered power from far-away elevations. The vertical IRF can be computed in a closed form through $|\mathbf{h}_{\mathrm{BF}}|^2$. In the ideal case of regularly spaced baselines, $|\mathbf{h}_{\mathrm{BF}}|^2$ is a squared periodic-sinc function, its first zero being placed at $2\pi/k_{z\max}$; the period of $|\mathbf{h}_{\mathrm{BF}}|^2$ is given by $2\pi/k_{z\min}$. The latter is the tomographic equivalent of the height of ambiguity for the interferometric case.

The large main lobe of $|\mathbf{h}_{\mathrm{BF}}|^2$ and slow decay of its response make beamforming unsuitable when the resolution along the elevation has priority. In this case, a different nonparametric model may be used: the Capon spectral estimator. The measured MB vector $\mathbf{y}$ is correlated to a signal that has a nonidentity covariance matrix, as shown in (6). Hence, the filter-design problem in (7) is revised as:

$$\mathbf{h}_{\mathrm{CP}} = \min_{\mathbf{h}} \mathbf{h}^{\dagger}\mathbf{R}\mathbf{h} \quad \text{s.t.} \quad \mathbf{h}^{\dagger}\mathbf{a}(z_l) = 1. \tag{9}$$

The resulting Capon filter and corresponding intensity are computed according to the following equations:

$$\mathbf{h}_{\mathrm{CP}} = \left[\mathbf{a}^{\dagger}(z_l)\mathbf{R}^{-1}\mathbf{a}(z_l)\right]^{-1}\mathbf{R}^{-1}\mathbf{a}(z_l), \tag{10}$$

and

$$\mathbf{P}_{\mathrm{CP}}(z_l) = \left[\mathbf{a}^{\dagger}(z_l)\mathbf{R}^{-1}\mathbf{a}(z_l)\right]^{-1}. \tag{11}$$

The expression in (11) is also known as the *Capon vertical-power spectrum*. The inversion in (11) is responsible for sharp peaks in the correspondence of the elevations where targets are present. However, the MB covariance matrix $\mathbf{R}$ is not known and must be estimated from the data itself. This goal is usually achieved by hypothesizing the ergodicity and spatial stationarity, but the limited number of looks can lead to instable inversions; this may be regularized by considering large estimation windows or introducing an extra noise term to the estimated $\mathbf{R}$ to avoid very small eigenvalues. The same considerations about the periodicity of the beamforming spectrum apply to $\mathbf{h}_{\mathrm{CP}}$ as well; in fact, specifying the resolution is more difficult, as it depends on the signal-to-noise ratio (SNR). Despite this uncertainty, the Capon estimator may still be preferred. The limit case is represented by the European Space Agency's BioSAR *2008* data set [34], where the resolution of the beamforming algorithm was often larger than the forest layer itself. Even in this extreme scenario, the Capon technique provided excellent 3D reconstruction [30]. Whenever radiometric accuracy is the main concern, the beamforming algorithm should be used instead. Many works relating tomographic backscattering intensity to forest biomass were based on beamforming, with the baseline distribution enabling proper imaging (an approximately 15-m vertical resolution for the TropiSAR data set [35]).

The two methods mentioned here rely on the linearization of the interferometric phase with respect to the elevation. This approximation is good for short baselines and as long as the vertical displacement from the linearization point is small compared to the distance of the target. However, the airborne-survey geometry of acquisition often makes this approximation unsuitable. In such cases, the back-projection tomographic algorithm [13] may be used in place of the beamforming technique. The back-projection method estimates the reflectivity of any point in the 3D space by compensating for the signal's delay (the time of arrival and phase value) for all available sensors. The use of the exact distances does not imply any linearization and produces clearer reconstructions. A further advantage of this framework involves the possibility of taking different propagation velocities into account, such as properly imaging targets that are buried in snow and ice [36].

The vertical power spectra of the vegetation layer that are returned by beamforming or the Capon technique reveal the 3D structure of the forest and underlying topography. Figure 2 provides an example of 3D reconstructions using the AfriSAR P band and UAVSAR L band above La Lopé, Gabon. In particular, the height-range tomograms are reported in HH polarization for the specified range line. Details about polarizations will be provided in the next section. Theoretically, the ground reflectivity in the tomogram is particularly visible when using low-frequency waves and in the case of sparse forests. Otherwise, the vegetation's attenuation can extinguish the signal beforehand; in this case, the peak associated with the ground in the tomogram loses power and may fade away. This is particularly evident

in the Capon reconstruction, where the ground is hardly detectable in the L band case [Figure 2(c)] compared to the P band version [Figure 2(d)]. Although this feature has the greatest impact on the ground backscattering, it influences the tomographic reconstruction of any target below the vegetation's top layer.

The complex vertical-reflectivity profile $|\boldsymbol{\gamma}|^2$ in (6) refers to the contribution that actually returns to the radar, thus incorporating any power loss due to propagation. Any quantitative evaluation of the reflectivity estimated through tomography should take this issue into account. Ideally, the attenuation of each vegetation layer should be known and compensated for; however, a direct estimation from the data represents a strongly ill-posed problem. Similar considerations apply for structural estimations, as any "hole" in the forest might be due to the strong attenuation of the targets above. This problem is less dramatic when using the HH polarimetric channel or very low-frequency signals. In such cases, due to the lower attenuation, the forest layer can be imaged from the top to bottom, thus offering the possibility of locating the top and bottom edges to estimate the underlying topography and forest height.

POLARIMETRIC TOMOSAR

In this section, some standard processes for the characterization of forest environments through polarimetric TomoSAR (PolTomoSAR) are reviewed. The polarization diversity in TomoSAR is expected to enhance focusing ability and facilitate the characterization of the electromagnetic (EM) behavior of complex media's different components.

Generally, the polarization information contained in the waves backscattered from the scene is known to be related to geometrical structure and orientation as well as the structures of the observed objects [37]. In particular, radar polarimetry employs the full-vector nature of polarized EM signals; by striking a wave to an object, the previously mentioned characteristic target information can be represented in a 2 × 2 scattering matrix, $\mathbf{S}$. In the case of having horizontally (h) or vertically (v) polarized antennas, and on the basis of (h, v), the fully polarimetric response from the target in a specific azimuth-range resolution cell can be given by

$$\mathbf{S} = \begin{bmatrix} \gamma_{hh} & \gamma_{hv} \\ \gamma_{vh} & \gamma_{vv} \end{bmatrix}, \tag{12}$$

where the complex scattering coefficient γ_{pq} indexed as $p, q = (h, v)$ represents the EM signal and is emitted through the polarization channel q and received on channel p. In the case of interchanging the transmitting and receiving antennas' roles, such as with the reciprocity theorem, the scattering matrix is symmetric; that is, $\gamma_{hv} = \gamma_{vh}$ [38].

In polarimetric SAR (PolSAR), $\mathbf{S}$ may be vectorized as the two known target scattering vectors; that is, the Pauli ($\mathbf{k}$) and lexicographic ($\boldsymbol{\Omega}$) feature vectors which are given by

$$\begin{aligned} \mathbf{k} &= \frac{1}{\sqrt{2}}[\gamma_{hh} + \gamma_{vv} \;\; \gamma_{hh} - \gamma_{vv} \;\; 2\gamma_{hv}]^T = s\mathbf{v}_k, \\ \boldsymbol{\Omega} &= [\gamma_{hh} \;\; \sqrt{2}\,\gamma_{hv} \;\; \gamma_{vv}]^T = s\mathbf{v}_\Omega, \end{aligned} \tag{13}$$

where $\sigma = |s|^2$ denotes the polarimetric span or reflectivity of the scatterer and $\mathbf{v}_k, \mathbf{v}_\Omega \in \mathbb{C}^{3\times 1}$ are unitary polarimetric target vectors; that is, $\mathbf{v}_k^\dagger \mathbf{v}_k = 1$ and $\mathbf{v}_\Omega^\dagger \mathbf{v}_\Omega = 1$. The deterministic scatterers' complete process can be described by $\mathbf{k}$ and $\boldsymbol{\Omega}$, while, for the naturally distributed scatterers present in forested areas, the target vectors may follow a random property if the wavelength of the SAR system is smaller than that of the resolution cell. For this case, the target vectors can be modeled by the complex circular Gaussian probability-density function, where the second-order statistic can be represented by the polarimetric coherence, $\mathbf{T} = E\{\mathbf{k}\mathbf{k}^\dagger\}$, and covariance, $\mathbf{C} = E\{\boldsymbol{\Omega}\boldsymbol{\Omega}^\dagger\}$, matrices.

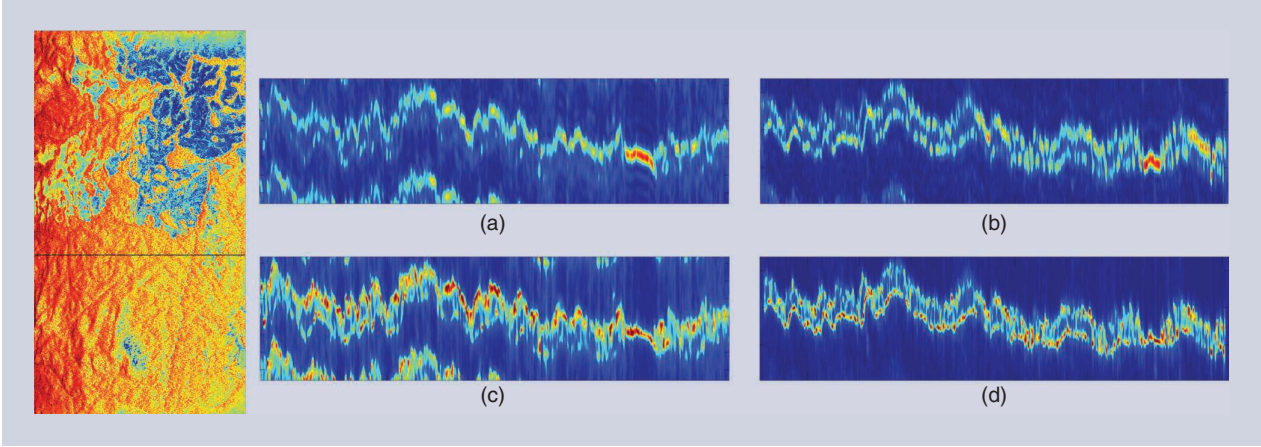

FIGURE 2. (a) The reconstructed tomograms for the specified range line in HH polarization for the L band with a beamforming solution. (b) The reconstructed tomograms for the specified range line in HH polarization for the P band with a beamforming solution. (c) The reconstructed tomograms for the specified range line in HH polarization for the L band with a Capon solution. (d) The reconstructed tomograms for the specified range line in HH polarization for the P band with Capon solution.

POLTOMOSAR SIGNAL MODEL

Using the PolTomoSAR configuration, the MB polarimetric target vectors can be formed by staking the TomoSAR responses in each polarimetric channel as $\mathbf{y}_p = [\mathbf{y}_1\ \mathbf{y}_2\ \mathbf{y}_3] \in \mathbb{C}^{3N\times 1}$, where $\mathbf{y}_i \in \mathbb{C}^{N\times 1}$ represents the MB data-stack vector in a specific channel i. It should be noted that $\mathbf{y}_p$ can be generated in either the Pauli or lexicographic representation. Using this representation convention, the TomoSAR equation in (4) can be extended to the polarimetric case as

$$\mathbf{y}_p = \mathbf{A}(\mathbf{z}, \mathbf{V})\mathbf{s} + \mathbf{w}_p \in \mathbb{C}^{3N\times 1}, \tag{14}$$

where $\mathbf{A}(\mathbf{z}, \mathbf{V}) = [\mathbf{a}(z_1, \mathbf{v}_{p1}), ..., \mathbf{a}(z_L, \mathbf{v}_{pL})] \in \mathbb{C}^{3N\times L}$ is the polarimetric steering matrix with $V = [\mathbf{v}_{p1}, ..., \mathbf{v}_{pL}]$, with $\mathbf{v}_{pl}$ being the unitary polarimetric target vector of the lth scatterer situated at elevation z_l. In particular, the polarimetric steering vector of the lth source is given by $\mathbf{a}(z_l, \mathbf{v}_{pl}) = \mathbf{v}_{pl} \otimes \mathbf{a}(z_l) = \mathbf{B}(z_l)\mathbf{v}_{pl}$, where $\otimes$ is the Kronecker product. It is noteworthy that the unitary target vector $\mathbf{v}_{pl}$ follows the polarimetric basis used to express $\mathbf{y}_p$.

Moreover, $\mathbf{s} \in \mathbb{C}^{L\times 1}$ and $\mathbf{w}_p \in \mathbb{C}^{3N\times 1}$ are the realization of the complex polarimetric response of the superimposed scatterers and additive noise, respectively. The complex additive noise is assumed to follow a Gaussian distribution with zero mean and a standard deviation of σ_{w_p}. The covariance matrix of $\mathbf{y}_p$ is generally given by

$$\mathbf{R}_p = E\{\mathbf{y}_p\mathbf{y}_p^\dagger\} = \mathbf{A}(\mathbf{z}, \mathbf{V})\mathrm{diag}\{|\mathbf{s}|^2\}\mathbf{A}(\mathbf{z}, \mathbf{V})^\dagger + \sigma_{w_p}^2\mathbf{I}. \tag{15}$$

POLTOMOSAR FOCUSING APPROACHES

Polarimetric tomography aims to retrieve the reflectivity and polarimetric scattering mechanism of the observed scatterers by the inversion of (15). Similar to the case of single polarization, PolTomoSAR reconstruction can be performed in the context of spectral estimation. Both of the widely used approaches that can connect with distributed media, i.e., beamforming and the Capon spectral estimator, can be extended to PolTomoSAR. In analogy, the aim of polarimetric beamforming and the polarimetric Capon spectral estimator is to find a filter that maximizes the reflectivity from a desired scatterer while rejecting the reflectivity from other scatterers. To do this, in optimization problems (7) and (9), the steering vector, $\mathbf{a}(z_l)$, is replaced by the polarimetric steering vector, $\mathbf{a}(z_l, \mathbf{v}_{pl})$. The polarimetric beamforming and Capon optimization problems are given by [9], [11], [14]

$$\mathbf{h}_{\mathrm{BF}} = \min_{\mathbf{h}} \mathbf{h}^\dagger\mathbf{h} \quad \text{s.t.} \quad \mathbf{h}^\dagger\mathbf{a}(z_l, \mathbf{v}_{pl}) = 1, \tag{16}$$

and

$$\mathbf{h}_{\mathrm{CP}} = \min_{\mathbf{h}} \mathbf{h}^\dagger\mathbf{R}_p\mathbf{h} \quad \text{s.t.} \quad \mathbf{h}^\dagger\mathbf{a}(z_l, \mathbf{v}_{pl}) = 1. \tag{17}$$

It can be shown that the reconstructed power of the signal from the solution of the optimization problems is polarization-dependent. However, the objective of PolTomoSAR is the estimation of the reflectivity's largest local maxima; following eigenvalue problems, the polarimetric spectrum can be reconstructed in 1D elevation space as [9], [11], [14]

$$P_{\mathrm{BF}}^p(z_l) = \frac{\lambda_{\max}(\mathbf{B}^\dagger(z_l)\mathbf{R}_p\mathbf{B}(z_l))}{N^2}, \tag{18}$$

and

$$P_{\mathrm{CP}}^p(z_l) = \frac{1}{\lambda_{\min}(\mathbf{B}^\dagger(z_l)\mathbf{R}_p^{-1}\mathbf{B}(z_l))}. \tag{19}$$

It is worth noting that the physical behavior of the reflector can be represented using the unitary polarimetric scattering patterns $\mathbf{e}_{\max}$ and $\mathbf{e}_{\min}$ for beamforming- and

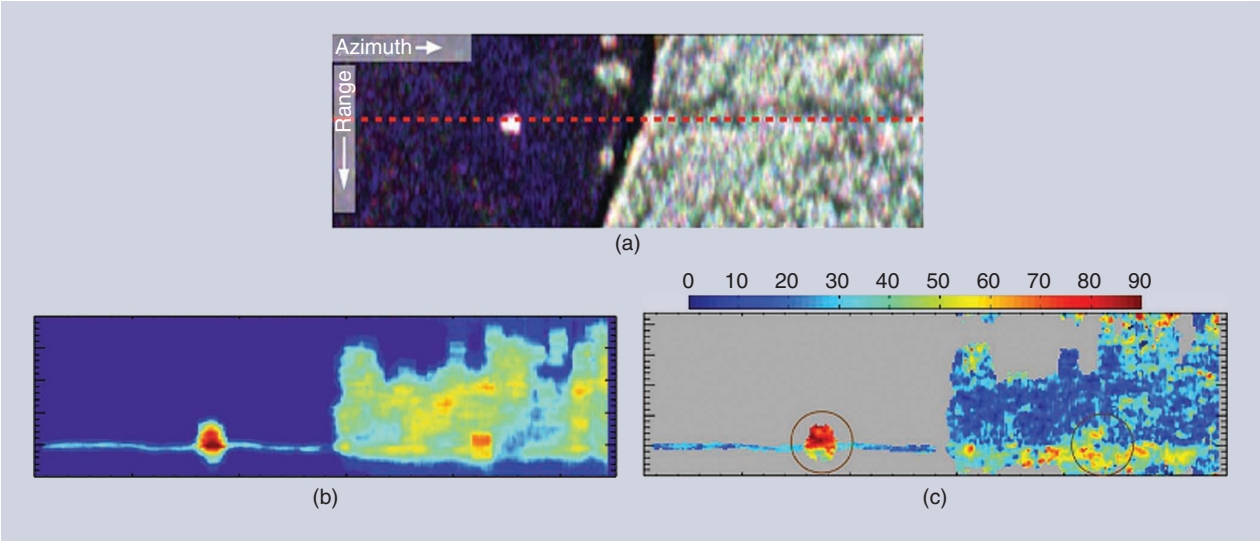

FIGURE 3. The polarimetrc MB data across the Dornstetten test site. (a) The Pauli image. (b) The polarimetric Capon tomogram. (c) The α-angle tomogram.

Capon-based reconstruction, respectively, in which $(\lambda_{\max}, \mathbf{e}_{\max})$ and $(\lambda_{\min}, \mathbf{e}_{\min})$ are the maximum and minimum eigenvalues and their corresponding eigenvectors.

The polarimetric Capon-based reconstruction application example is given using polarimetric L band airborne data acquired by the German Aerospace Center's Experimental SAR system above a Dornstetten, Germany, test site (see Figure 3). The MB data from 23 flight tracks were obtained. The baselines form a quasi-uniform linear array with an average baseline close to 20 m, and the geometric vertical resolution is approximately 2 m. The considered transect line for PolTomoSAR reconstruction contains under-foliage objects (trucks). The tomogram of the polarimetric reflectivity in the elevation-azimuth plane is shown in Figure 3(b), where the forest profiles (end of azimuth line) and truck shape were extracted through the Capon estimation approach. Taking the reconstructed unitary polarimetric-scattering pattern, the estimated α tomogram is reported as well. The truck outside the forest was identified with strong double-bounce reflection at the ground-truck interaction, and the one beneath the canopy was reconstructed with the higher α values.

In the case of full-rank polarimetric information and aiming for a second-order polarimetric-information reconstruction (that is, the polarimetric coherence, **T**, and covariance, **C**, matrices), the model given in (14) may be replaced by

$$\mathbf{y}_p = \sum_{l=1}^{L} \mathbf{X}_p(z_l) \otimes \mathbf{a}(z_l)\mathbf{a}^{\dagger}(z_l) + \mathbf{w}_p, \tag{20}$$

where $\mathbf{X}_p(z_l) = E\{|s(z_l)|^2 \mathbf{v}_{pl}\mathbf{v}_{pl}^{\dagger}\} \in \mathbb{C}^{3\times 3}$ is the second-order polarimetric coherence or the covariance matrix (depending on the generation form of $\mathbf{y}_p$) of the scatterer at elevation z_l. In such a case, $\mathbf{X}_p$ can be retrieved using the following full-rank reconstructions:

$$\begin{aligned} \mathbf{X}_{p_{\mathrm{BF}}}(z_l) &= \mathbf{B}^{\dagger}(z_l)\mathbf{R}_p\mathbf{B}(z_l), \\ \mathbf{X}_{p_{\mathrm{CP}}}(z_l) &= (\mathbf{B}^{\dagger}(z_l)\mathbf{R}_p^{-1}\mathbf{B}(z_l))^{-1}. \end{aligned} \tag{21}$$

In (21), $\mathbf{X}_{p_{\mathrm{BF}}}$ and $\mathbf{X}_{p_{\mathrm{CP}}}$ are positive semidefinite matrices that can be characterized through any classical polarimetric-processing algorithms, such as three-component Freeman–Durden decomposition [39].

TomoSAR and PolTomoSAR reconstructions can be performed in a sparse-based framework. Sparsity-based retrieval is able to enhance the reconstruction quality with respect to beamforming and the Capon spectral estimator. The sparsity-based full-rank polarimetric reconstruction of the coherence/covariance matrix was presented in [16]. Figure 4 provides an example of full-rank reconstruction through different methods. In particular, an experiment is performed that involves the Freeman–Durden decomposition in the elevation slant-range plan using TropiSAR data [35]. The color-coded tomograms are generated through three extracted features of the decomposition, where the double-bounce, volumetric, and surface scatterings are set as red, green, and blue, respectively. It is interesting to observe that the ground is mainly detected by the double-bounce scattering mechanism, while, in the upper forest layer and canopy, volumetric scattering is dominant, as expected. The resolution improvement from the sparsity-based technique is evident.

POLARIMETRIC BACKSCATTERING SEPARATION

In addition to the reconstruction algorithm's effectiveness, the separation and characterization of superimposed scatterers highly depends on the MB SAR sensor configuration. Typically, decomposition is an alternative approach that may provide a promising solution in the scattering-mechanism separation. The scattering-mechanism decomposition effectiveness in PolSAR [40], [41] and polarimetric interferometric SAR (PolInSAR) [42] images has already been proved. With respect to polarimetric MB data, different processing strategies have been presented in the literature [17]–[19]; among them, one widely used

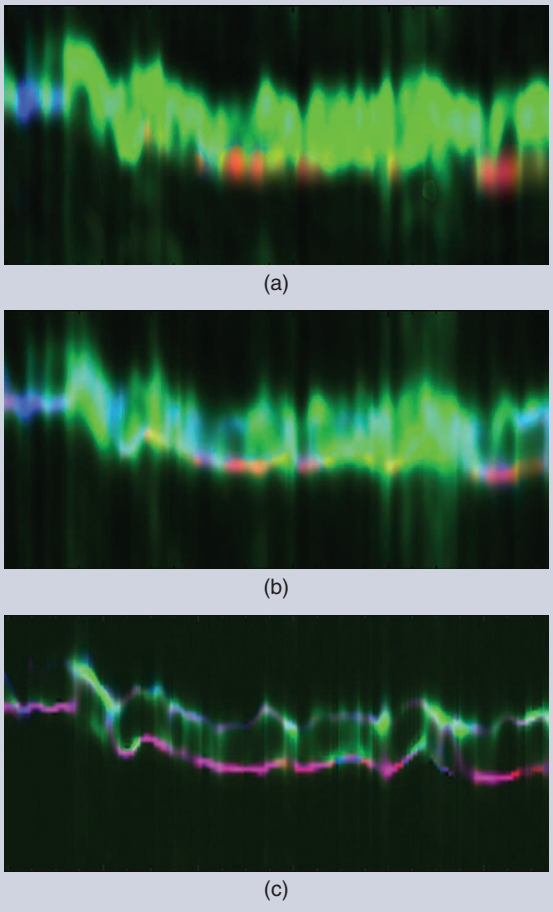

FIGURE 4. The color-coded Freeman–Durden tomograms extracted through full-rank reconstruction approaches. The (a) beamforming-, (b) Capon-, and (c) sparsity-based approaches. The horizontal and vertical axes of the tomograms are related to the slant range and elevation directions.

approach is the sum of Kronecker products (SKP) [17], which provides the basis for the decomposition of the MB data from a forested area along the elevation direction. The method models the polarimetric radar backscattering from the ground and canopy layers in forested areas. Suppose that the polarimetric MB covariance matrix ($\mathbf{R}_p$) is estimated from the generated lexicographic target vector, $\mathbf{y}_p$; the method then expresses $\mathbf{R}_p$ by the KP between two matrices, which is obtained by singular-value decomposition; that is,

$$\mathbf{R}_p = \sum_{j=1}^{2} \tilde{\mathbf{R}}_j \otimes \tilde{\mathbf{C}}_j, \tag{22}$$

where $\tilde{\mathbf{C}}_j \in \mathbb{C}^{3\times 3}$ and $\tilde{\mathbf{R}}_j \in \mathbb{C}^{N\times N}$ account for the correlation among different polarizations and baselines, respectively. It can be shown that the matrices $\tilde{\mathbf{C}}_j$ and $\tilde{\mathbf{R}}_j$ are related to the polarimetric covariance matrix, $(\mathbf{C}_g, \mathbf{C}_v)$, and interferometric structure matrix, $(\mathbf{R}_g, \mathbf{R}_v)$, of the ground and aboveground volumetric scattering from the canopy via a linear invertible transformation as

$$\begin{aligned}
\mathbf{R}_g &= a\tilde{\mathbf{R}}_1 + (1-a)\tilde{\mathbf{R}}_2 \\
\mathbf{R}_v &= b\tilde{\mathbf{R}}_1 + (1-b)\tilde{\mathbf{R}}_2 \\
\mathbf{C}_g &= \frac{1}{a-b}((1-b)\tilde{\mathbf{C}}_1 - b\tilde{\mathbf{C}}_2) \\
\mathbf{C}_v &= \frac{1}{a-b}(-(1-a)\tilde{\mathbf{C}}_1 + a\tilde{\mathbf{C}}_2),
\end{aligned} \tag{23}$$

where a and b are two real numbers obtained by requiring the semipositive definitiveness condition in the previous linear equations. The polarimetric matrices of $\mathbf{C}_g$ and $\mathbf{C}_v$ represent information from the backscattering mechanisms about the ground and volume, respectively, while matrices $\mathbf{R}_g$ and $\mathbf{R}_v$ contain interferometric information that can be employed for height mapping and the reconstruction of the vertical structure. The results of SKP decomposition using BioSAR 2007 data [34] are shown in Figure 5. The tomograms are reconstructed using the decomposed $\mathbf{R}_g$ and $\mathbf{R}_v$.

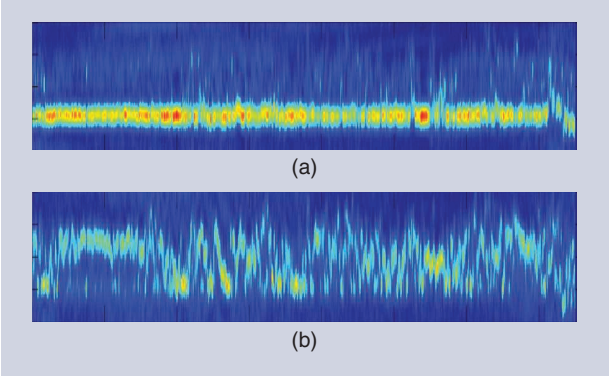

FIGURE 5. The Capon-based tomograms of (a) the ground and (b) the volume obtained by SKP decomposition. The horizontal and vertical axes of the tomograms are related to the slant range and elevation directions.

INHERENT DIFFICULTIES OF TOMOSAR

The principle of TomoSAR is similar to that of X-ray computed tomography (CT). However, compared with CT, the application of TomoSAR is limited by some additional problems. First, while a sufficient number of uniformly distributed sensors is available in CT, the number of MB SAR data sources is generally limited in TomoSAR, with only a relatively low number of available passes, which do not necessarily provide regular sampling. Moreover, MB TomoSAR data acquisitions may span a long interval, which could cause an unavoidable temporal decorrelation and the appearance of disturbances due to atmospheric variations. Furthermore, the focusing procedure given with the TomoSAR equation in (4) might be affected by a phase error because of the real tracks' deviation from the nominal positions. These issues can impair focusing and 3D-information extraction. They and their possible effects must be considered when MB SAR data are processed. More details of these issues and the possible remedies are discussed next.

NONOPTIMAL MB CONFIGURATION

In CT applications, a narrow X-ray beam is transmitted for a set of angle positions that are 360° around the object; in TomoSAR, under realistic conditions, acquiring the equally spaced baselines may not be feasible. Moreover, due to some practical limitations, only a relatively small number of passes and trajectories is available. In practice, and more specifically in the spaceborne case, the MB data are obtained through irregular sampling and a small number of baselines. This problem introduces a degree of ill-conditioning into the inversion process, and it may lead to ambiguities in the reconstruction [10].

Generally, the MB data-sampling distance must be sufficiently small to fulfill the Nyquist criterion for the spatial bandwidth of $\mathbf{y}$; otherwise, as in the case of azimuth focusing, the occurrence of sidelobes and ambiguities in the reconstruction is inevitable. The optimal sampling distance (d_{opt}) between tracks depends on the slant range and target height (H) and can be represented as [6]

$$d_{\text{opt}} \leq \frac{\lambda r}{H}. \tag{24}$$

In such a case, the total number of required baselines might be obtained by dividing the overall baseline, B_n, by the optimal sampling distance. The TomoSAR-achievable vertical resolution is highly dependent on the extension of the tomographic aperture (B_n). Although it may not always be possible for TomoSAR users to design the optimal MB configuration for the sampling, resolution, and number of images, some feasible strategies might be useful to mitigate a nonoptimal configuration's blurring and sidelobe effects. The baseline interpolation [21], in which a set of uniform baseline data is recovered from the available nonuniform baseline, may enhance the reconstruction quality for typical approaches, such as beamforming and the Capon spectral estimator.

Another possibility is to employ more effective reconstruction approaches, including sparsity-based techniques such as compressive sensing [43], [44]. These techniques aim to reconstruct the vertical reflectivity, on the condition that the signal is sparse along the elevation. The sparse representation of distributed media in the elevation dimension can be exploited in the wavelet domain. The most important characteristic of these approaches concerns the possibility to achieve super-resolution capability even with a reduced number of irregular passes.

PHASE ERROR

Another issue that may limit TomoSAR processing involves the presence of phase error between the acquisition tracks. In TomoSAR, it is assumed that the phase of the complex backscattered signal relies only on the nominal sensor-to-target distance. Practically, phase error impairs the interferometric MB data and causes the measured phase to deviate from the real one. The appearance of phase error or disturbances in TomoSAR is due either to the atmospheric variations from track to track or the residual platform-motion errors caused by the inability of the employed navigation equipment to precisely measure the flight trajectory to subwavelength accuracy. The former is more significant in the case of spaceborne data acquisition, while the latter is mainly related to airborne systems. It is relevant to show that both cases disturb the TomoSAR equation in a same way, as

$$\mathbf{y} = \exp(i\phi_E)\boldsymbol{A}(z)\boldsymbol{\gamma} + \mathbf{w}, \tag{25}$$

where ϕ_E is an $N \times 1$ phase vector whose dependence on each azimuth-range pixel and baseline is understood. Generally, phase error is statistically modeled as a set of independent (across the different acquisitions) random variables. Theoretically, possible effects ranging from high sidelobes to totally defocused signals may arise from the inversion of (25). This problem causes critical issues that impair any extracted information. As noted in [25], dealing with natural distributed targets that have a low SNR can intensify the phase error's harmful effect.

The TomoSAR phase-error problem can be tackled by estimating ϕ_E and employing the result in the inversion of tomographic problem (25). Different types of algorithms can be used for estimating ϕ_E, providing a well-focused tomographic reconstruction. The classical approaches make use of permanent scatterers (PSs) and distributed (surface) scatterers. These techniques assume a constant or very slowly varying phase error for the whole image scene [22]. The reflectivity profile for the selected PS can be modeled ideally as the Dirac delta function. Accordingly, (25) can be written by $\mathbf{y} = \exp(\phi_E)\mathbf{a}(z_0)$, where z_0 is the elevation of the PS. By adopting a reference system that has its origin in the position of the selected PS, the phase error can be set equal to the phase vector of the selected PS pixel for each baseline. The method's performance may deteriorate with the distance from the reference target. In addition, the detection of suitable PSs in forest environments might be challenging, especially when operating with high-frequency images.

For different approaches presented in literature, readers can refer to [24], [45], and [46]. However, a more efficient algorithm can be found in [23]; this method calibrates the MB data by jointly estimating the platform-positioning errors and elevation of the targets in the scene. Scenario-independent, pixel-by-pixel phase-error estimation was proposed in [25] by sharpening the focused signal and obeying a zero-phase derivative (with respect to the baseline) constraint. This estimation problem is conveniently formulated by assuming the second-phase derivatives as unknowns and twice integrating them for obtaining the calibration-phase values. Figure 6 offers an example of the results that were obtained by using this method with TropiSAR data [35] before and after the phase-error compensation. The Capon-based tomograms are given for a fixed-range line in HV polarization. Sidelobes and the defocusing effect of the phase error can be readily seen without compensation; they are suppressed after calibration.

TEMPORAL DECORRELATION

Temporal decorrelation constitutes a particular criticality in the development of spaceborne missions for forest tomography. Its source can be related to weather conditions, such as wind, that induce motion in the natural scatterers and to the vegetation growth that can occur during a long interval (a few months). Moreover, irrigation, rain, and soil moisture as well as droughts can introduce more complex effects on the multitemporal MB data [47].

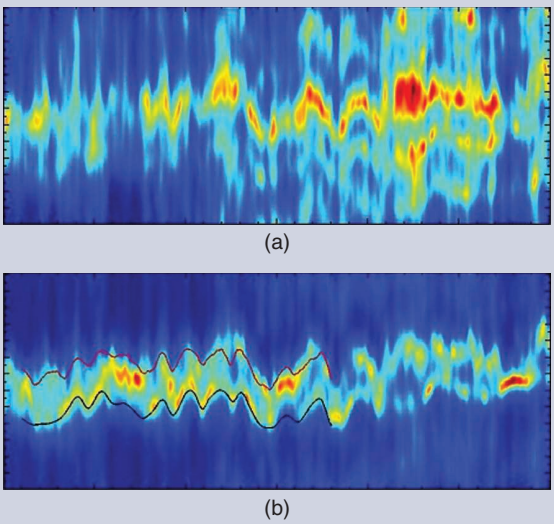

FIGURE 6. The capon-based tomogram (a) before and (b) after phase calibration. The horizontal and vertical axes of the tomograms are related to the azimuth and elevation directions. The black and red lines represent lidar-based ground- and canopy-height models.

Temporal decorrelation has been known since the beginning of repeat-pass interferometry. With reference to TomoSAR, one of the first attempts at analyzing the temporal decorelation effect was performed in [26], where the decorrelation effect was simulated by the Brownian motion of the scatterers. Analysis of the repeat-pass scenario has shown that the temporal-decorrelation effect, even at a mild temporal baseline (a few weeks), appears to be a critical factor [48]. Theoretically, natural scatterers' temporal-coherence loss, which is due to their geometrical and dielectric variation in the interferometric time interval, leads to some blurring and defocusing in the temporal synthesis of the elevation array.

Many studies have been dedicated to analyzing the effects of temporal decorrelation with respect to the employed frequency [49], [50] and polarization [51] of the data set. As evidenced in the literature, lower-frequency data have demonstrated more robustness against temporal decorrelation, while polarizations that indicate double-bounce and surface scattering mechanisms are expected to be more robust than those sensitive to volumetric scattering. A detailed analysis of the polarization basis in the presence of temporal decorrelation can be found in [51].

One possible way to mitigate the decorrelation effect is to consider the advanced SAR system configurations that have insignificant temporal baselines. However, through the long duration of spaceborne data acquisitions, a specific processing step should be performed during the TomoSAR inversion. Theoretically, temporal decorrelation induces spreading in the temporal-frequency domain; consequently, the temporal bandwidth of the signal may characterize the temporal decorrelation's behavior and effect. The typical array-processing methods based on deterministic scatterer assumptions, such as beamforming and the Capon spectral estimator, are affected by such a dispersion, and their results may be significantly affected by such a mismatch.

The framework of generalized focusing has proved to be effective in focusing the spread signal by taking dispersion into account [52]. With reference to TomoSAR applications, the concept of generalization is extended to differential tomography, to cope with the signal spreading along the temporal frequency, using generalized multiple-signal classification (MUSIC) [27] and generalized Capon-based [28] approaches. Figure 7 presents sample experimental results that confirm the potential of the generalized-focusing approach using BioSAR 2007 data [34]. Visual inspection shows the improvement in the reconstruction of the upper layers of the forest that was obtained by generalized Capon methods. Dealing with a spatially distributed forest environment, Capon-based focusing approaches may be preferred to MUSIC.

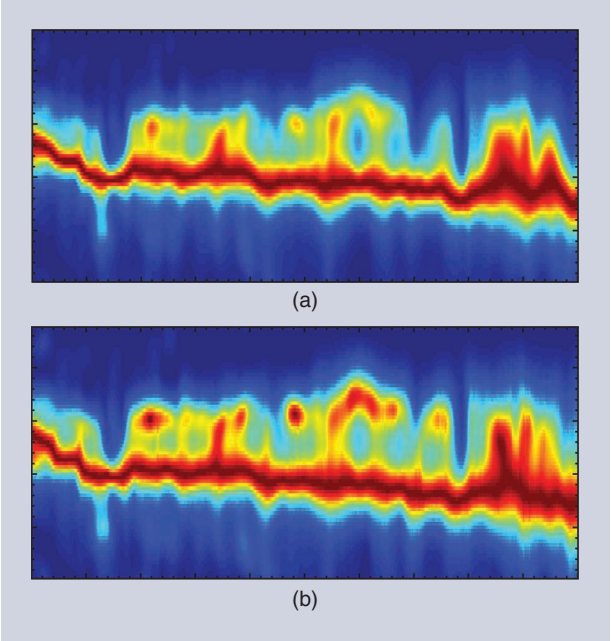

FIGURE 7. The BioSAR 2007 transect tomogram in HV polarization obtained in a zero temporal frequency. The (a) classical Capon and (b) generalized Capon approach. The horizontal and vertical axes of the tomograms are related to the slant range and elevation directions.

APPLICATION EXAMPLES

TomoSAR provides access to the vertical structure of an extended, semitransparent medium. This implies that the upper part of the target backscatters a portion of the signal power; still, a significant fraction keeps propagating so that echoes produced by underlying features can be received. The transparency property of any target is dependent on the wavelength used to image it. Many natural targets are suitable for a tomographic analysis using microwaves: deserts, vegetation, snow packs, and glaciers [53], [54]. Snowpack thickness has been mapped through the localization of the air-snow and snow-ice interfaces; these interfaces can be properly imaged when their propagation speed is used to compensate for the phase delays during the tomographic focusing. As a consequence, the permittivity was estimated with the vertical structure [55].

The possibility of monitoring the temporal evolution of both features was demonstrated in [56]. On glaciers, the possibility of monitoring the temporal evolution of the ice mass was demonstrated in [36] through a similar procedure. The very high quality of the airborne 3D reconstruction proved to be comparable to the one obtained with a much smaller-scale instrument functioning as a ground-penetrating radar. Arid regions' good penetration characteristic makes them a perfect environment for tomographic mapping; however, no works exist at the present time. Great effort has been made to interpret tomographic data from forests, resulting in many products, some of which are described here.

Two main feature classes can be extracted by analyzing tomographic stacks gathered on forests: structural parameters and dielectric properties (Figure 8). The proper imaging of the vegetation layer from top to bottom gives straightforward access to the ground topography [31], [32] and forest

height [57]. The latter was properly retrieved on managed and unmanaged forests of different kinds, from boreal to tropical [30], [31]. Forest height represents an important biophysical parameter whose global monitoring is gaining attention; moreover, it is the main input of many allometric relationships that reveal further features of the forest. The ground topography below the forest layer can also be regarded as an independent product; however, it provides access to a deeper analysis of the trees. Locating the ground position enables tomography to focus on specific elevations defined with respect to the ground level. This possibility was exploited in [29], where the backscattered power coming from 30 m above the ground level was successfully related to the forest biomass.

After ground localization, the spatial distribution of the tomographic profiles has been found to be related to large-scale forest properties. In particular, it was employed as a proxy for the growth stage and horizontal homogeneity of the forest [7], complementary to the vertical characterization [58]. The separation of the scattering mechanisms based on their elevation eases their interpretation, too. The complex behavior of backscattering from the ground level can be analyzed alone against the ground slope to reveal the physical properties of the forest [33].

CONCLUSIONS

The 3D imaging that uses SAR tomographic focusing is an efficient and powerful way to overcome the severe limitations of 2D scanning for the characterization of volumetric environments. Due to the intrinsic cylindrical ambiguity of SAR imaging, characterizing volumetric media from their SAR reflectivity reveals a difficult and extremely badly conditioned problem. By coherently combining a set of SAR images acquired from close positions, TomoSAR permits the retrieval of an environment's reflectivity and distribution in the elevation direction. TomoSAR has been successfully applied to 3D analysis of urban areas, snow and ice packs, and forested environments. From the retrieved vertical-reflectivity profiles, various works showed that it is possible to estimate the extent and structure of media, detect objects and layers, and estimate velocity profiles. Polarimetric diversity may be combined with TomoSAR to characterize scattering mechanisms in 3D and to separate media that should not be discriminated by using spatial diversity alone.

The different results for TomoSAR proposed in the literature were derived from ground data acquired by ground-based and airborne SAR sensors. The application of TomoSAR using spaceborne data is hindered by the fact that different baselines are usually acquired at time lags on the order of days, limiting the analysis to temporally stable targets, such as those encountered in urban scenarios. A possible solution consists of using single-pass interferometers, as in the case of Tandem-X, as well as currently operating and possible future systems, such as [59] and [60], together with dedicated signal processing techniques.

The tandem-like or correlation tomographic configuration is sketched in Figure 9. Each pair of interferometric images is acquired nearly simultaneously and, hence, not affected by temporal decorrelation the way repeat-pass measures would be with a spatial baseline that varies from one visit to the other. The resulting tomographic process is intrinsically robust to temporal decorrelation, leading to a

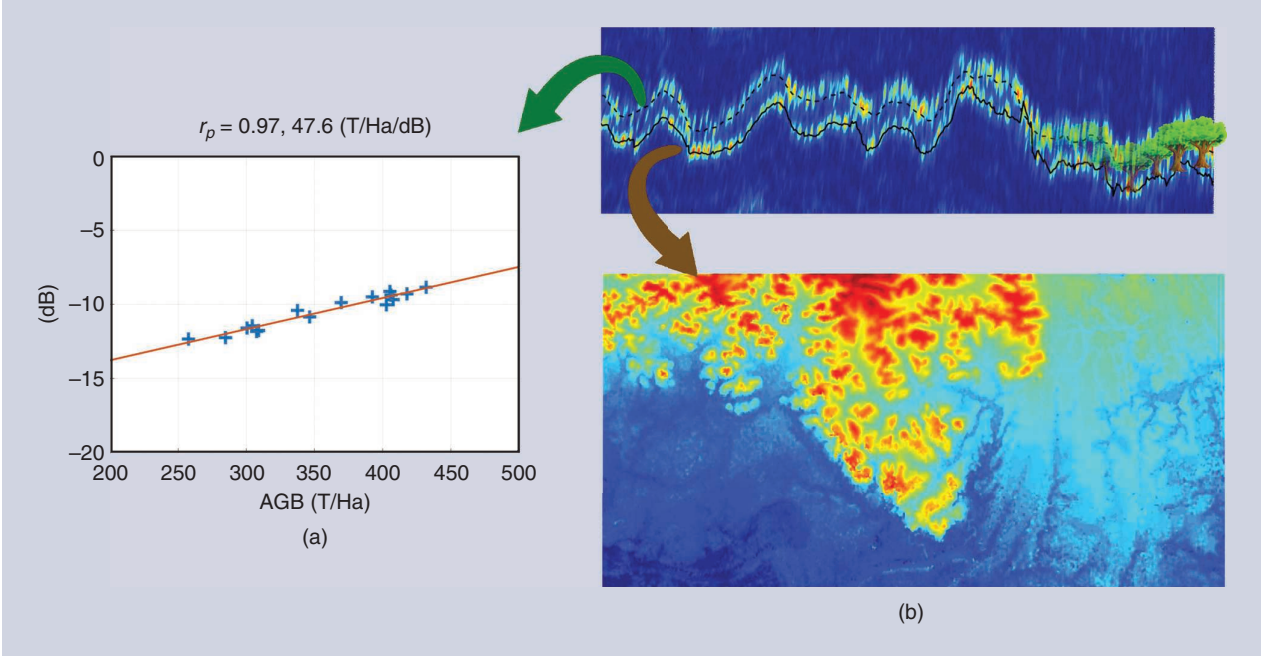

FIGURE 8. The application of TomoSAR in ground-height mapping and biomass estimation. (a) The AGB. (b) The ground topography.

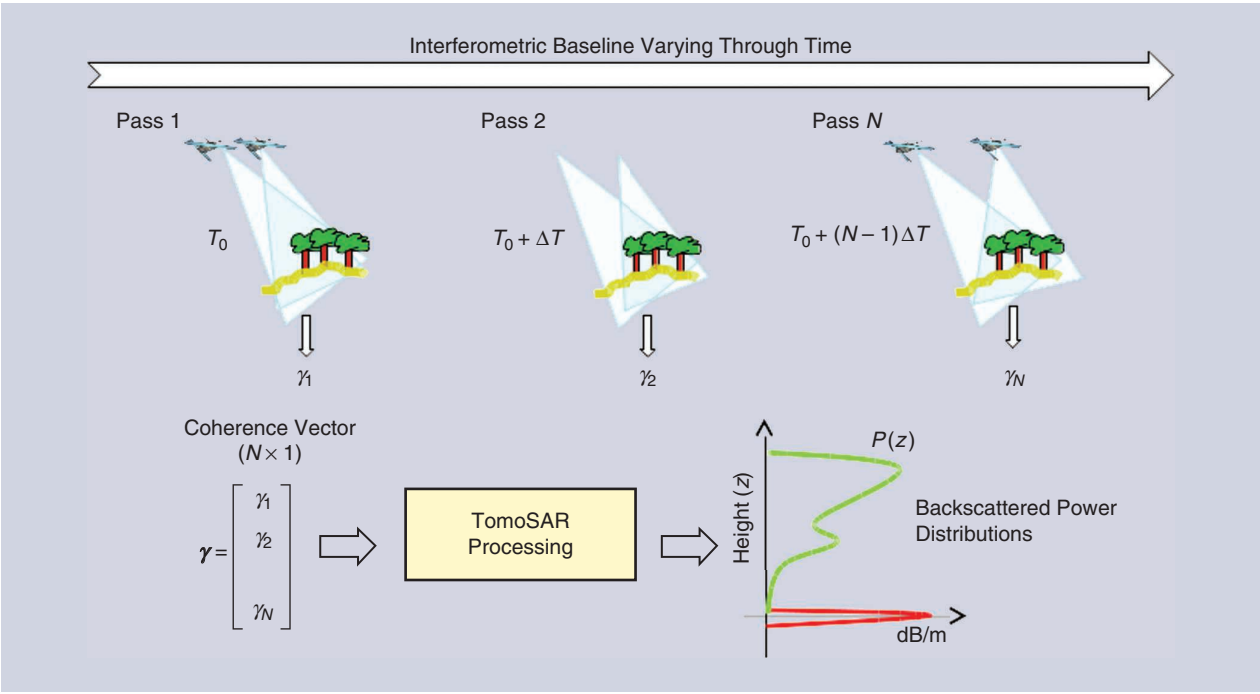

FIGURE 9. The tandem-like acquisition configuration and tomographic processing.

potential solution for the 3D imaging of natural environments from space. The main difference among the classical, repeat-pass, and correlation tomographic modes relates to the constraint they impose on the duration of the acquisition of the tomographic stack of SAR images. In the repeat-pass tomographic mode, this duration should be inferior to the correlation time of the SAR signal, that is, the time lag during which speckled responses remain correlated. In a correlation-tomography configuration, the duration compares to the time after which scene's mean reflectivity cannot be considered as stationary.

ACKNOWLEDGMENT

The authors wish to thank Dr. Marco Lavalle of the NASA Jet Propulsion Laboratory, Pasadena, California, for providing the UAVSAR tomograms included in this article.

AUTHOR INFORMATION

Hossein Aghababaei (aghababaee@uniparthenope.it) received his M.Sc. and Ph.D. degrees in remote sensing in 2011 and 2017, respectively. From 2017 to 2019, he was employed as a research fellow at the Department of Engineering, Università di Napoli Parthenope, Italy. Currently, he is an assistant professor with the University of Twente, Faculty of Geo-Information Science and Earth Observation, Department of Earth Observation Science Enschede, The Netherlands. His main research interests are in synthetic-aperture radar (SAR) tomographic, target scattering decomposition, and polarimetric SAR processing for multidimensional geophysical information extraction. He is a Member of the IEEE.

Giampaolo Ferraioli (giampaolo.ferraioli@uniparthenope.it) received his B.S. and M.S. degrees and his Ph.D. degree in telecommunication engineering from the Università degli Studi di Napoli Parthenope, Italy, in 2003, 2005, and 2008, respectively. Currently, he is an assistant professor with the Università degli Studi di Napoli Parthenope. His main research interests include statistical signal and image processing, radar systems, synthetic aperture radar interferometry, image restoration, and magnetic resonance imaging. In 2009, he won the IEEE 2009 Best European Ph.D. Thesis in Remote Sensing Prize, sponsored by the IEEE Geoscience and Remote Sensing Society. He serves as an associate editor of *IEEE Geoscience and Remote Sensing Letters*, and he is on the editorial boards of *IEEE Geoscience and Remote Sensing Letters* and MDPI's *Remote Sensing*. He is member of the technical liaison committee for *IEEE Transactions on Computational Imaging*. He is a Senior Member of the IEEE.

Laurent Ferro-Famil (laurent.ferro-famil@univ-rennes1.fr) received his laurea degree in electronics systems and computer engineering and his M.S. and Ph.D. degrees in electronics from the University of Nantes, France, in 1996, 1996, and 2000, respectively. He has been a full professor with the University of Rennes 1, France, since 2011, where he was an associate professor in 2001 and is currently the head of the Remote Sensing Department, Institute of Electronics and Telecommunications of Rennes. His current activities in education are concerned with analog electronics, digital communications, microwave theory, signal processing, and polarimetric synthetic-aperture radar (SAR) remote sensing. His current research interests include polarimetric SAR signal statistical processing, radar polarimetry

theory, and natural media remote sensing using multibaseline polarimetric SAR interferometry data, with applications to classification, electromagnetic scattering modeling and physical parameter retrieval, time-frequency analysis, and 3D reconstruction of environments using tomography. He is a Member of the IEEE.

Yue Huang (yue.huang@univrennes1.fr) received her M.Sc. degree in electronics, electrical engineering, and automation and systems from the University Paul Sabatier, Toulouse, France, in 2007 and her Ph.D. degree in signal processing and telecommunications from the University of Rennes 1, France, in 2011. She is currently with at the Institute of Electronics and Telecommunications of Rennes. From 2011 to 2015, she was a senior scientist at Intermap Technologies Corp., Calgary, Canada. She has been involved in many R&D projects of synthetic-aperture radar (SAR) imaging and its applications. Her research interests include polarimetric SAR interferometry techniques, SAR interferometry and differential interferometry, physical parameter retrieval, 3D environment reconstruction, target detection, SAR signal processing, SAR tomography, multivariate spectral estimation methods, and blind source separation.

Mauro Mariotti d'Alessandro (mauro.mariotti@polimi.it) received his bachelor's, master's, and Ph.D. degrees in telecommunications engineering from the Politecnico di Milano, Italy, in 2005, 2009, and 2014, respectively. From 2014 to 2016, he was part of the research team of the Comisión Nacional de Actividades Espaciales. Since 2016, he has been a research assistant with the Department of Electronics, Informatics, and Bioengineering of the Politecnico di Milano. He is currently working on the development of algorithms for the European Space Agency BIOMASS system. His research interests include synthetic-aperture radar tomography, polarimetry, and calibration of airborne and spaceborne data. He is a Member of the IEEE.

Vito Pascazio (vito.pascazio@uniparthenope.it) graduated summa cum laude in electronic engineering from the Università di Bari, Italy, in 1986. In 1990, he received his Ph.D. degree in electronic engineering and computer science from the Department of Electronic Engineering, Università di Napoli Federico II, Napoli, Italy. Currently, he is a full professor at the Università di Napoli Parthenope, Italy. His research interests include remote sensing, image processing, and linear and nonlinear estimation, with particular emphasis in image computing and processing and reconstruction of microwave and radar images. He has published more than 180 technical papers. In 1990, he was awarded the Philip Morris Prize for Scientific and Technological Research. In 2015, he was a general cochair of the IEEE International Geoscience and Remote Sensing Symposium conference. He is a Senior Member of the IEEE.

Gilda Schirinzi (gilda.schirinzi@uniparthenope.it) graduated cum laude in electronic engineering at the University of Naples Federico II. Since 2008, she has been at the University of Naples "Parthenope," Italy. From 1985 to 1986, she was at the European Space Agency, European Space Research and Technology Centre, Noordwijk, The Netherlands. In 1988, she joined the Istituto di Ricerca per l'Elettromagnetismo e i Componenti Elettronici, Naples. In 1998, she joined the University of Cassino as an associate professor of telecommunications, and in 2005 she became a full professor. Her main scientific interests are in the field of signal processing for remote sensing applications, with particular reference to synthetic aperture radar interferometry and tomography. She is a Senior Member of the IEEE.

Stefano Tebaldini (stefano.tebaldini@polimi.it) received his M.S. degree in telecommunication engineering and his Ph.D. degree from the Politecnico di Milano, Italy, in 2005 and 2009, respectively. Since 2005, he has been with the Digital Signal Processing Research Group, Politecnico di Milano, where he is currently an associate professor. He has been a key scientist in several studies with the European Space Agency (ESA), concerning the tomographic phase of the BIOMASS mission. He was a member of the SAOCOM-CS Expert Group, ESA. He is one of the inventors of a new technology patented by T.R.E. for the exploitation of multiple interferograms in the presence of distributed scattering. He teaches courses on signal theory and remote sensing at the Politecnico di Milano. His research interests include Earth observation with synthetic aperture radar and radar design and processing. He is a Senior Member of the IEEE.

REFERENCES

[1] P. O. Eugene, "Relationships between structure and function in the ecosystem," *Jpn. J. Ecol.*, vol. 12, no. 3, pp. 108–118, 1962. doi: 10.18960/seitai.12.3_108.

[2] A. Boncina, "Comparison of structure and biodiversity in the Rajhenav virgin forest remnant and managed forest in the Dinaric region of Slovenia," *Glob. Ecol. Biogeogr.*, vol. 9, no. 3, pp. 201–211, 2000. doi: 10.1046/j.1365-2699.2000.00155.x.

[3] B. S. Hardiman, G. Bohrer, C. M. Gough, C. S. Vogel, and P. S. Curtis, "The role of canopy structural complexity in wood net primary production of a maturing northern deciduous forest," *Ecology*, vol. 92, no. 9, pp. 1818–1827, 2011. doi:10.1890/10-2192.1.

[4] H. T. Ishii, S-i Tanabe, and T. Hiura, "Exploring the relationships among canopy structure, stand productivity, and biodiversity of temperate forest ecosystems," *For. Sci.*, vol. 50, no. 3, pp. 342–355, 2004. doi: 10.1093/forestscience/50.3.342.

[5] S. Frolking, M. W. Palace, D. Clark, J. Q. Chambers, H. Shugart, and G. C. Hurtt, "Forest disturbance and recovery: A general review in the context of spaceborne remote sensing of impacts on aboveground biomass and canopy structure," *J. Geophys. Res. Biogeosci.*, vol. 114, no. G2, 2009. doi: 10.1029/2008JG000911.

[6] A. Reigber and A. Moreira, "First demonstration of airborne SAR tomography using multibaseline L-band data," *IEEE Trans. Geosci. Remote Sens.*, vol. 38, no. 5, pp. 2142–2152, Sept. 2000. doi: 10.1109/36.868873.

[7] M. Tello, V. Cazcarra-Bes, M. Pardini, and K. Papathanassiou, "Forest structure characterization from SAR tomography at L-band," *IEEE J. Sel. Topics Appl. Earth Observ. Remote Sens.*, vol. 11, no. 10, pp. 3402–3414, Oct. 2018. doi: 10.1109/JSTARS.2018.2859050.

[8] S. Tebaldini, "Forest structure retrieval from multi-baseline SARS," in *Remote Sensing of Biomass – Principles and Applications*, L. Fatoyinbo, Ed. London: IntechOpen, 2012.

[9] L. Ferro-Famil, Y. Huang, and E. Pottier, "Principles and applications of polarimetric SAR tomography for the characterization of complex environments," in *Proc. VIII Hotine-Marussi Symp. Mathematical Geodesy*. New York: Springer-Verlag, 2015, pp. 243–255. doi: 10.1007/1345_2015_12.

[10] G. Fornaro, F. Lombardini, and F. Serafino, "Three-dimensional multipass SAR focusing: Experiments with long-term spaceborne data," *IEEE Trans. Geosci. Remote Sens.*, vol. 43, no. 4, pp. 702–714, Apr. 2005. doi: 10.1109/TGRS.2005.843567.

[11] S. Sauer, L. Ferro-Famil, A. Reigber, and E. Pottier, "Three-dimensional imaging and scattering mechanism estimation over urban scenes using dual-baseline polarimetric InSAR observations at L-band," *IEEE Trans. Geosci. Remote Sens.*, vol. 49, no. 11, pp. 4616–4629, Nov. 2011. doi: 10.1109/TGRS.2011.2147321.

[12] F. Gini, F. Lombardini, and M. Montanari, "Layover solution in multibaseline SAR interferometry," *IEEE Trans. Aerosp. Electron. Syst.*, vol. 38, no. 4, pp. 1344–1356, Oct. 2002. doi: 10.1109/TAES.2002.1145755.

[13] O. Frey and E. Meier, "3-D time-domain SAR imaging of a forest using airborne multibaseline data at L- and P-bands," *IEEE Trans. Geosci. Remote Sens.*, vol. 49, no. 10, pp. 3660–3664, Oct. 2011. doi: 10.1109/TGRS.2011.2128875.

[14] Y. Huang, L. Ferro-Famil, and A. Reigber, "Under-foliage object imaging using SAR tomography and polarimetric spectral estimators," *IEEE Trans. Geosci. Remote Sens.*, vol. 50, no. 6, pp. 2213–2225, June 2012. doi: 10.1109/TGRS.2011.2171494.

[15] L. Ferro-Famil, Y. Huang, and S. Tebaldini, "Polarimetric characterization of 3-D scenes using high-resolution and full-rank polarimetric tomographic SAR focusing," in *Proc. IEEE Int. Geoscience and Remote Sensing Symp. (IGARSS)*, July 2016, pp. 5694–5697. doi: 10.1109/IGARSS.2016.7730487.

[16] H. Aghababaee, G. Ferraioli, L. Ferro-Famil, G. Schirinzi, and Y. Huang, "Sparsity based full rank polarimetric reconstruction of coherence matrix T," *Remote Sens.*, vol. 11, no. 11, p. 1288, 2019. doi: 10.3390/rs11111288. [Online]. Available: https://www.mdpi.com/2072-4292/11/11/1288

[17] S. Tebaldini, "Algebraic synthesis of forest scenarios from multibaseline PolInSAR data," *IEEE Trans. Geosci. Remote Sens.*, vol. 47, no. 12, pp. 4132–4142, Dec. 2009. doi: 10.1109/TGRS.2009.2023785.

[18] M. Neumann, L. Ferro-Famil, and A. Reigber, "Estimation of forest structure, ground, and canopy layer characteristics from multibaseline polarimetric interferometric SAR data," *IEEE Trans. Geosci. Remote Sens.*, vol. 48, no. 3, pp. 1086–1104, Mar. 2010. doi: 10.1109/TGRS.2009.2031101.

[19] H. Aghababaee and M. R. Sahebi, "Model-based target scattering decomposition of polarimetric SAR tomography," *IEEE Trans. Geosci. Remote Sens.*, vol. 56, no. 2, pp. 972–983, Feb. 2018. doi: 10.1109/TGRS.2017.2757062.

[20] M. Pardini and K. Papathanassiou, "On the estimation of ground and volume polarimetric covariances in forest scenarios with SAR tomography," *IEEE Geosci. Remote Sens. Lett.*, vol. 14, no. 10, pp. 1860–1864, Oct. 2017. doi: 10.1109/LGRS.2017.2738672.

[21] F. Lombardini and M. Pardini1, "First experiments of sector interpolated SAR tomography," in *Proc. IEEE Int. Geoscience and Remote Sensing Symp.*, July 2010, pp. 21–24. doi: 10.1109/IGARSS.2010.5654011.

[22] S. Tebaldini and A. Monti Guarnieri, "On the role of phase stability in SAR multibaseline applications," *IEEE Trans. Geosci. Remote Sens.*, vol. 48, no. 7, pp. 2953–2966, July 2010. doi: 10.1109/TGRS.2010.2043738.

[23] S. Tebaldini, F. Rocca, M. Mariotti d'Alessandro, and L. Ferro-Famil, "Phase calibration of airborne tomographic SAR data via phase center double localization," *IEEE Trans. Geosci. Remote Sens.*, vol. 54, no. 3, pp. 1775–1792, Mar. 2016. doi: 10.1109/TGRS.2015.2488358.

[24] G. Gatti, S. Tebaldini, M. Mariotti d'Alessandro, and F. Rocca, "Algae: A fast algebraic estimation of interferogram phase offsets in space-varying geometries," *IEEE Trans. Geosci. Remote Sens.*, vol. 49, no. 6, pp. 2343–2353, June 2011. doi: 10.1109/TGRS.2010.2091278.

[25] H. Aghababaee, G. Fornaro, and G. Schirinzi, "Phase calibration based on phase derivative constrained optimization in multibaseline SAR tomography," *IEEE Trans. Geosci. Remote Sens.*, vol. 56, no. 11, pp. 6779–6791, Nov. 2018. doi: 10.1109/TGRS.2018.2843447.

[26] F. Lombardini and H. Griffiths, "Effect of temporal decorrelation on 3D SAR imaging using multiple pass beamforming," in *Proc. IEE/EUREL Meeting Radar and Sonar Signal Processing*, 1998, pp. 1–4.

[27] F. Lombardini and F. Cai, "Temporal decorrelation-Robust SAR tomography," *IEEE Trans. Geosci. Remote Sens.*, vol. 52, no. 9, pp. 5412–5421, Sept. 2014. doi: 10.1109/TGRS.2013.2288689.

[28] H. Aghababaee, G. Ferraioli, and G. Schirinzi, "Differential SAR tomography reconstruction robust to temporal decorrelation effects," *IEEE Trans. Geosci. Remote Sens.*, vol. 57, no. 11, pp. 9071–9080, Nov. 2019. doi: 10.1109/TGRS.2019.2924738.

[29] D. Ho Tong Minh, T. L. Toan, F. Rocca, S. Tebaldini, M. M. d'Alessandro, and L. Villard, "Relating P-band synthetic aperture radar tomography to tropical forest biomass," *IEEE Trans. Geosci. Remote Sens.*, vol. 52, no. 2, pp. 967–979, Feb. 2014. doi: 10.1109/TGRS.2013.2246170.

[30] S. Tebaldini and F. Rocca, "Multibaseline polarimetric SAR tomography of a boreal forest at P- and L-bands," *IEEE Trans. Geosci. Remote Sens.*, vol. 50, no. 1, pp. 232–246, Jan. 2012. doi: 10.1109/TGRS.2011.2159614.

[31] M. Pardini, J. S. Kim, K. Papathanassiou, and I. Hajnsek, "3-D structure observation of African tropical forests with multibaseline SAR: Results from the AfriSAR campaign," in *Proc. IEEE Int. Geoscience and Remote Sensing Symp. (IGARSS)*, July 2017, pp. 4288–4291. doi: 10.1109/IGARSS.2017.8127950.

[32] M. Mariotti d'Alessandro and S. Tebaldini, "Digital terrain model retrieval in tropical forests through P-band SAR tomography," *IEEE Trans. Geosci. Remote Sens.*, vol. 57, no. 9, pp. 6774–6781, 2019. doi: 10.1109/TGRS.2019.2908517.

[33] M. M. d'Alessandro, S. Tebaldini, and F. Rocca, "Phenomenology of ground scattering in a tropical forest through polarimetric synthetic aperture radar tomography," *IEEE Trans. Geosci. Remote Sens.*, vol. 51, no. 8, pp. 4430–4437, Aug. 2013. doi: 10.1109/TGRS.2013.2246573.

[34] I. Hajnsek et al., "BioSAR 2007 technical assistance for the development of airborne SAR and geophysical measurements during the BioSAR 2007 experiment: Final report without synthesis," ESA Contract, No. 20755/07, 2008.

[35] P. C. Dubois-Fernandez et al., "The TropiSAR airborne campaign in French Guiana: Objectives, description, and observed temporal behavior of the backscatter signal," *IEEE Trans. Geosci. Remote Sens.*, vol. 50, no. 8, pp. 3228–3241, Aug. 2012. doi: 10.1109/TGRS.2011.2180728.

[36] S. Tebaldini, T. Nagler, H. Rott, and A. Heilig, "Imaging the internal structure of an alpine glacier via L-band airborne SAR tomography," *IEEE Trans. Geosci. Remote Sens.*, vol. 54, no. 12, pp. 7197–7209, Dec. 2016. doi: 10.1109/TGRS.2016.2597361.

[37] S. Cloude, *Polarisation: Applications in Remote Sensing*. London: Oxford Univ. Press, 2010.

[38] J.-S. Lee and E. Pottier, *Polarimetric Radar Imaging: From Basics to Applications*. Boca Raton, FL: CRC, 2009.

[39] A. Freeman and S. L. Durden, "A three-component scattering model for polarimetric SAR data," *IEEE Trans. Geosci. Remote Sens.*, vol. 36, no. 3, pp. 963–973, May 1998. doi: 10.1109/36.673687.

[40] S. R. Cloude and E. Pottier, "A review of target decomposition theorems in radar polarimetry," *IEEE Trans. Geosci. Remote Sens.*, vol. 34, no. 2, pp. 498–518, 1996. doi: 10.1109/36.485127.

[41] H. Aghababaee and M. R. Sahebi, "Incoherent target scattering decomposition of polarimetric SAR data based on vector model roll-invariant parameters," *IEEE Trans. Geosci. Remote Sens.*, vol. 54, no. 8, pp. 4392–4401, Aug. 2016. doi: 10.1109/TGRS.2016.2540807.

[42] K. P. Papathanassiou and S. R. Cloude, "Single-baseline polarimetric SAR interferometry," *IEEE Trans. Geosci. Remote Sens.*, vol. 39, no. 11, pp. 2352–2363, Nov. 2001. doi: 10.1109/36.964971.

[43] E. Aguilera, M. Nannini, and A. Reigber, "Wavelet-based compressed sensing for SAR tomography of forested areas," in *Proc. EUSAR 9th European Conf. Synthetic Aperture Radar*, Apr. 2012, pp. 259–262.

[44] Y. Huang, J. Levy-Vehel, L. Ferro-Famil, and A. Reigber, "Three-dimensional imaging of objects concealed below a forest canopy using SAR tomography at L-band and wavelet-based sparse estimation," *IEEE Geosci. Remote Sens. Lett.*, vol. 14, no. 9, pp. 1454–1458, Sept. 2017. doi: 10.1109/LGRS.2017.2709839.

[45] A. Reigber, P. Prats, and J. J. Mallorqui, "Refined estimation of time-varying baseline errors in airborne SAR interferometry," *IEEE Geosci. Remote Sens. Lett.*, vol. 3, no. 1, pp. 145–149, Jan. 2006. doi: 10.1109/LGRS.2005.860482.

[46] M. Pardini and K. Papathanassiou, "A two-step phase calibration method for tomographic applications with airborne SAR data," in *Proc. EUSAR 10th European Conf. Synthetic Aperture Radar*, June 2014, pp. 1–4.

[47] M. Lavalle, M. Simard, and S. Hensley, "A temporal decorrelation model for polarimetric radar interferometers," *IEEE Trans. Geosci. Remote Sens.*, vol. 50, no. 7, pp. 2880–2888, July 2012. doi: 10.1109/TGRS.2011.2174367.

[48] D. Ho Tong Minh, S. Tebaldini, F. Rocca, and T. Le Toan, "The impact of temporal decorrelation on biomass tomography of tropical forests," *IEEE Geosci. Remote Sens. Lett.*, vol. 12, no. 6, pp. 1297–1301, June 2015. doi: 10.1109/LGRS.2015.2394235.

[49] Y. Morishita and R. F. Hanssen, "Temporal decorrelation in L-, C-, and X-band satellite radar interferometry for pasture on drained peat soils," *IEEE Trans. Geosci. Remote Sens.*, vol. 53, no. 2, pp. 1096–1104, Feb. 2015. doi: 10.1109/TGRS.2014.2333814.

[50] H. Joerg, M. Pardini, I. Hajnsek, and K. P. Papathanassiou, "First multi-frequency investigation of SAR tomography for vertical structure of agricultural crops," in *Proc. EUSAR 10th European Conf. Synthetic Aperture Radar*, June 2014, pp. 1–4.

[51] H. Aghababaee, G. Ferraioli, and G. Schirinzi, "Polarization analysis of the impact of temporal decorrelation in synthetic aperture radar (SAR) tomography," *Remote Sens.*, vol. 11, no. 6, p. 686, 2019. doi: 10.3390/rs11060686.

[52] S. Valaee, B. Champagne, and P. Kabal, "Parametric localization of distributed sources," *IEEE Trans. Signal Process.*, vol. 43, no. 9, pp. 2144–2153, Sept. 1995. doi: 10.1109/78.414777.

[53] T. G. Yitayew, L. Ferro-Famil, T. Eltoft, and S. Tebaldini, "Lake and fjord ice imaging using a multifrequency ground-based tomographic SAR system," *IEEE J. Sel. Topics Appl. Earth Observ. Remote Sens.*, vol. 10, no. 10, pp. 4457–4468, Oct. 2017. doi: 10.1109/JSTARS.2017.2718998.

[54] B. Rekioua, M. Davy, L. Ferro-Famil, and S. Tebaldini, "Snowpack permittivity profile retrieval from tomographic SAR data," *Comptes Rendus Physique*, vol. 18, no. 1, pp. 57–65, 2017. doi: 10.1016/j.crhy.2015.12.016.

[55] D. Ho Tong Minh et al., "Vertical structure of P-band temporal decorrelation at the Paracou forest: Results from TropiScat," *IEEE Geosci. Remote Sens. Lett.*, vol. 11, no. 8, pp. 1438–1442, Aug. 2014. doi: 10.1109/LGRS.2013.2295165.

[56] O. Frey, C. L. Werner, R. Caduff, and A. Wiesmann, "A time series of tomographic profiles of a snow pack measured with SnowScat at X-/Ku-band," in *Proc. IEEE Int. Geoscience and Remote Sensing Symp. (IGARSS)*, July 2016, pp. 17–20. doi: 10.1109/IGARSS.2016.7728995.

[57] V. Wasik, P. C. Dubois-Fernandez, C. Taillandier, and S. S. Saatchi, "The AfriSAR campaign: Tomographic analysis with phase-screen correction for P-band acquisitions," *IEEE J. Sel. Topics Appl. Earth Observ. Remote Sens.*, vol. 11, no. 10, pp. 3492–3504, Oct. 2018. doi: 10.1109/JSTARS.2018.2831441.

[58] M. Pardini, M. Tello, V. Cazcarra-Bes, K. P. Papathanassiou, and I. Hajnsek, "L- and P-band 3-D SAR reflectivity profiles versus lidar waveforms: The AfriSAR case," *IEEE J. Sel. Topics Appl. Earth Observ. Remote Sens.*, vol. 11, no. 10, pp. 3386–3401, Oct. 2018. doi: 10.1109/JSTARS.2018.2847033.

[59] L. Ferro-Famil, Y. Huang, S. Tebaldini, and M. Azcueta, "Assessment of SAOCOM CS data processing for the characterization of forested areas using polarimetric SAR tomography," in *Proc. IEEE Int. Geoscience and Remote Sensing Symp. (IGARSS)*, July 2017, pp. 2468–2471. doi: 10.1109/IGARSS.2017.8127493.

[60] S. Tebaldini and L. Ferro-Famil, "SAR tomography from bistatic single-pass interferometers," in *Proc. IEEE Int. Geoscience and Remote Sensing Symp. (IGARSS)*, July 2017, pp. 133–136. doi: 10.1109/IGARSS.2017.8126912.

GRS